PAPER

Check for updates

MOF-derived MoO₂/C composites as high-performance electrodes for electrochemical uranium(VI) removal

Hongyan Zhou, [a] Ranran Jiao,[b] Xiaotong Ma,[a] Suyuan Zeng [*a] and Yuwei Mi*[a]

In this study, an octahedral MoO₂/C composite was synthesized by calcining a molybdenum-based metal–organic framework (MOF) precursor. This unique octahedral architecture significantly enhances the electro-adsorption performance while ensuring excellent structural stability. The optimized material exhibited a high U(VI) adsorption capacity of 806.79 mg g^{-1} from a 300 mg L^{-1} initial solution under an applied potential of 1.2 V for 5 h. Moreover, it demonstrated excellent cycling stability, maintaining a U(VI) removal rate above 65% even after ten consecutive adsorption–desorption cycles using 0.1 mol L^{-1} Na₂CO₃ as the eluent. This work provides a novel design strategy for developing high-capacity, stable electrode materials for efficient uranium electrosorption.

1. Introduction

Nuclear energy, characterized by its high energy density and low carbon emissions, is becoming indispensable in the global transition to low-carbon energy systems.[1,2] Uranium, as the essential fuel for nuclear fission, faces supply constraints stemming from the limited and geographically uneven distribution of terrestrial ores, casting doubt on the long-term viability of nuclear power.[3] In stark contrast, the world's oceans hold an estimated 4.5 billion metric tons of dissolved uranium—approximately a thousandfold greater than terrestrial reserves—representing an immense potential resource.[4] The extraction of uranium from seawater, however, faces formidable challenges. These arise principally from its ultra-trace concentration (∼3.3 ppb) and the concomitant radiological and chemical risks posed by uranium-laden process streams.[5,6] These challenges underscore the critical need for next-generation extraction technologies that exhibit both high efficiency and exceptional ion selectivity—properties essential for securing a sustainable uranium(VI) supply while mitigating secondary environmental contamination.[7]

In response to the limitations of conventional adsorption techniques, uranium extraction technology has evolved to encompass a spectrum of methods including ion exchange,[8] membrane separation,[9] photocatalysis[10] and electrochemical processes.[11] Among these, electrochemical approaches have

demonstrated particular promise. Under an applied electric field below 1.2 V, capacitive deionization (CDI) significantly enhances the migration and enrichment of uranyl ions within the electrical double layer.[12,13] More importantly, some electrode materials electrochemically reduce soluble U(VI) to insoluble uranium oxides, a mechanism that effectively overcomes the inherent capacity limitation of physical adsorption and substantially enhances extraction performance.

Despite significant progress in electrode material development, substantial challenges remain in achieving balanced comprehensive performance for practical uranium extraction. Zhang *et al.* developed a thermochemically synthesized amine-oxime-functionalized MOF with a U(VI) adsorption capacity of 684.93 mg g^{-1}, yet its multi-step synthesis—involving reflux, centrifugation, and repeated washing—poses scalability challenges.[14] Similarly, Adish Tyagi *et al.* reported a modified UIO-66-NH₂ (Ce) MOF that exhibits approximately 50% capacity loss after only 8 cycles, coupled with a complex synthesis procedure requiring ice-bath and reflux steps, limiting its practical applicability.[15] In another approach, Sun *et al.* prepared a cucurbituril-derived macroporous carbon with a capacity of 343.6 mg g^{-1} and a low normalized capacity of 4.70 μmol m^{-2}, reflecting the inherent limitation of macroporous structures in achieving high density of accessible adsorption sites.[16] These examples collectively underscore the ongoing need for adsorbents that integrate high capacity, long-term stability, and scalable synthesis.

The rational design of electrode architectures is crucial for advancing electrochemical uranium extraction technologies. While conventional materials—including carbon-based compounds,[17] COFs,[18] MXenes,[19] and polymer composites[20]—have been widely investigated, they face three interconnected challenges: limited ion transport efficiency due to high

aSchool of Chemistry and Chemical Engineering, Liaocheng University, Liaocheng 252059, China. E-mail: drzengsy@163.com; luckyyuweimi@163.com; Fax: +86-635-8230196; Tel: +86-635-8230614

bNational Synchrotron Radiation Laboratory, Anhui Provincial Engineering Laboratory of Advanced Functional Polymer Film, CAS Key Laboratory of Soft Matter Chemistry, University of Science and Technology of China, Hefei 230026, China

diffusion resistance, progressive capacity degradation during cycling, and interfacial instability between the electrode and electrolyte. These drawbacks collectively restrict their practical implementation in uranium recovery applications.

To address these challenges, self-supporting electrodes with rationally designed porous frameworks have emerged as a promising alternative. A representative example is the MoO_2/C composite prepared by pyrolyzing a molybdenum-based metal–organic framework (MOF) followed by Fe^{3+} etching. This material maintains the structural periodicity and porosity of its MOF precursor, forming an interconnected three-dimensional network that significantly promotes ion transport efficiency.[21] During the thermal treatment process, the metal nodes are *in situ* transformed into uniformly dispersed MoO_2 nanoparticles while the organic ligands convert into a continuous conductive carbon matrix. This unique "nanocage" architecture effectively confines the active particles to prevent aggregation, thereby ensuring high dispersion and thermodynamic stability of the active sites.[22] The synergistic combination of these characteristics—including the ordered porous structure for enhanced mass transfer, uniformly distributed MoO_2 nanoparticles providing abundant active sites, and the conductive carbon matrix ensuring structural integrity—collectively enables high-capacity and fast-kinetics uranium adsorption, establishing an ideal material platform for efficient electrochemical uranium extraction.[6]

Herein, by achieving atomic dispersion and encapsulation of non-coordinated POM clusters within organic ligands, this synthetic strategy enables homogeneous *in situ* reactions while confining carbonization to the organic ligands, thus preventing agglomeration of the resulting nanocrystals. As a proof-of-concept, we successfully fabricated MoO_2/C nanocomposites through a MOF-templated approach, which exhibit an exceptional uranyl adsorption capacity of up to 806.79 mg g^{-1} at an initial concentration of 300 mg L^{-1}, along with rapid adsorption kinetics in acidic aqueous media. Notably, the MoO_2/C composite was serendipitously obtained at a relatively low pyrolysis temperature of 600 °C, and its uranyl electro-adsorption behavior remains largely unexplored. Benefiting from its porous and robust architecture with ultrafine primary nanocrystals, the MoO_2/C octahedral structure displays exceptional adsorption performance under acidic conditions.

2. Experimental section

2.1. Preparation of MoO_2/C

Fig. 1 illustrates the synthesis of porous MoO_2/C nano-octahedra for efficient uranium adsorption. A unique MOF precursor, $[Cu_2(BTC)_{4/3}(H_2O)_2]_6[H_3PMo_{12}O_{40}]$ (NENU-5; BTC = benzene-1,3,5-tricarboxylate), was employed; this material is structurally analogous to HKUST-1 but contains periodically embedded Keggin-type polyoxometalates ($H_3PMo_{12}O_{40}$).

For NENU-5 synthesis, copper acetate (0.1997 g), L-glutamic acid (0.0735 g), and phosphomolybdic acid hydrate (0.3 g) were dissolved in 40 mL deionized water with stirring for 20 min. Separately, 1,3,5-benzenetricarboxylic acid (0.1408 g) was dissolved in 40 mL absolute ethanol. The solutions were combined, stirred for 14 h, and the resulting green precipitate was collected by centrifugation, washed thrice with ethanol, and dried overnight at 70 °C.

Pyrolysis of NENU-5 nano-octahedra under nitrogen at 600 °C (5 °C min^{-1}, 6 h) yielded MoO_2/C–Cu composites. During annealing, Mo-based POMs reacted with carbon from BTC ligands to form MoO_2/C nanocrystallites, while Cu^{2+} clusters reduced to metallic Cu. Final etching with aqueous $FeCl_3$ solution ($2 Fe^{3+} + Cu \rightarrow Cu^{2+} + 2 Fe^{2+}$) produced MoO_2/C nano-octahedra for uranium electro-adsorption.

2.2. CDI performance measurements for removal of U(vi)

The electroadsorption of U(vi) was performed using a custom-built capacitive deionization (CDI) system. The system configuration comprises two acrylic plates, two silicone spacers (1.0 mm thickness), two titanium current collectors, and a silicone gasket. For electrode preparation, the active materials (MoO_2/C cathode and activated carbon anode) were homogeneously mixed with acetylene black (AB) conductive additive and polyvinylidene fluoride (PVDF) binder at an 8 : 1 : 1 mass ratio in N-methylpyrrolidone (NMP) solvent to form a slurry. This slurry was uniformly coated onto titanium substrates and vacuum-dried at 70 °C for 12 hours, resulting in an active material loading of ~0.94 mg cm^{-2} (total ~15 mg per 16 cm^2 electrode area).
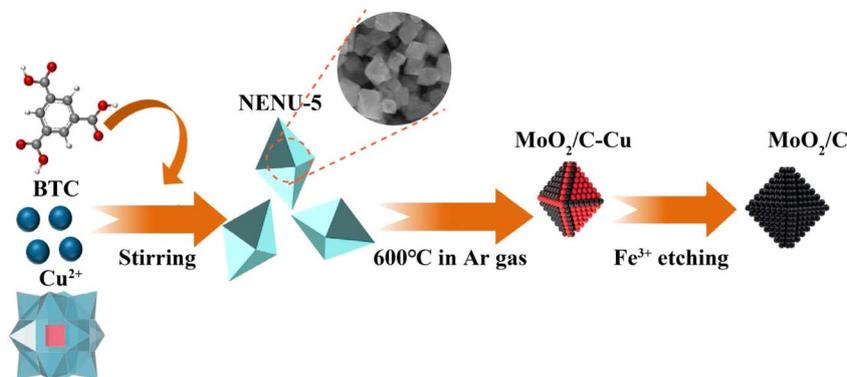

Fig. 1 Schematic illustration of synthesis process for MoO_2/C.

3. Results and discussion

3.1. Characterization of MoO₂/C composite

X-ray diffraction (XRD) analysis was conducted to characterize the crystallinity of the synthesized MoO₂/C composite. As shown in Fig. 2a, the XRD pattern reveals well-defined diffraction peaks at 18.45°, 26.03°, 37.02°, 53.51°, 60.20°, 66.66° and 78.49°, which are assigned to the (−101), (−111), (−211), (−312), (031), (−402) and (231) crystallographic planes of monoclinic MoO₂ (JCPDS No. 32-0671), respectively. The absence of any impurity-related diffraction peaks demonstrates the high phase purity of the N₂-annealed MoO₂/C product. The sharp peak profiles further confirm the high crystallinity of the material obtained at the annealing temperature of 600 °C. Moreover, the lack of discernible diffraction peaks corresponding to crystalline carbon indicates the amorphous nature of the carbon matrix in the composite.

The structural characteristics of the MoO₂/C composite were further investigated by Raman spectroscopy. As presented in Fig. 2b, the Raman spectrum displays two characteristic peaks at 1348 and 1590 cm^{-1}, which are attributed to the D band (associated with sp³-hybridized disordered carbon) and G band (representing sp²-hybridized graphitic carbon), respectively.[23–25] Quantitative analysis yields an I_D/I_G intensity ratio of 2.69, indicating a relatively low degree of graphitization in the carbon matrix. This observation is in excellent agreement with the XRD results, where the absence of crystalline carbon diffraction peaks corroborates the predominantly amorphous nature of the carbon component.

Fig. 2c shows the TGA curve of the MoO₂/C composite obtained under an air atmosphere. As shown in the TGA curve, the composite exhibited a weight loss of 1.63% within the temperature range of 30–200 °C, which can be assigned to the evaporation of water. From 200 to 520 °C, the carbon was oxidized. Above 600 °C, the weight loss proceeded at a relatively steady rate, which is solely attributed to the thermal stability of MoO₂. The FTIR spectra of MoO₂/C are shown in Fig. 2d. The absorption peaks at 1047 cm^{-1} and 812 cm^{-1} can be assigned to the vibrations of Mo=O and Mo–O species, respectively, confirming the presence of MoO₂ in MoO₂/C.[26] Collectively, the FTIR characterization reveals abundant hydroxyl groups (–OH) on the MoO₂/C surface.[27]

After the annealing and etching processes, the MoO₂/C sample is obtained as a black powder. As shown in Fig. 3a and b, the MoO₂/C composite material consists of numerous octahedral particles with sizes of approximately 250 nm. The octahedral MoO₂/C composite materials exhibit enhanced adsorbate interactions due to structural defects predominantly localized at the edges and corners of the octahedra. These defects disrupt chemical bond symmetry, elevate surface energy, and thereby strengthen interfacial affinity for adsorbates.[28] Secondly, the rigid octahedral framework of MoO₂/C mitigates agglomeration and maintains structural integrity under cyclic adsorption–desorption conditions. The regular geometric morphology of MoO₂/C octahedra with exposed high-activity crystal facets provides abundant adsorption sites, thereby enhancing capacitive deionization (CDI) performance.[29–31]

The detailed nanostructure of the as-prepared MoO₂/C was further measured by HRTEM. The image in Fig. 3c reveals well-defined lattice fringes with an interplanar spacing of 0.342 nm in the MoO₂ octahedron, corresponding to the (−111) crystallographic plane of monoclinic MoO₂ (JCPDS No. 32-0671). Fig. 3d shows the elemental mapping images of the MoO₂/C
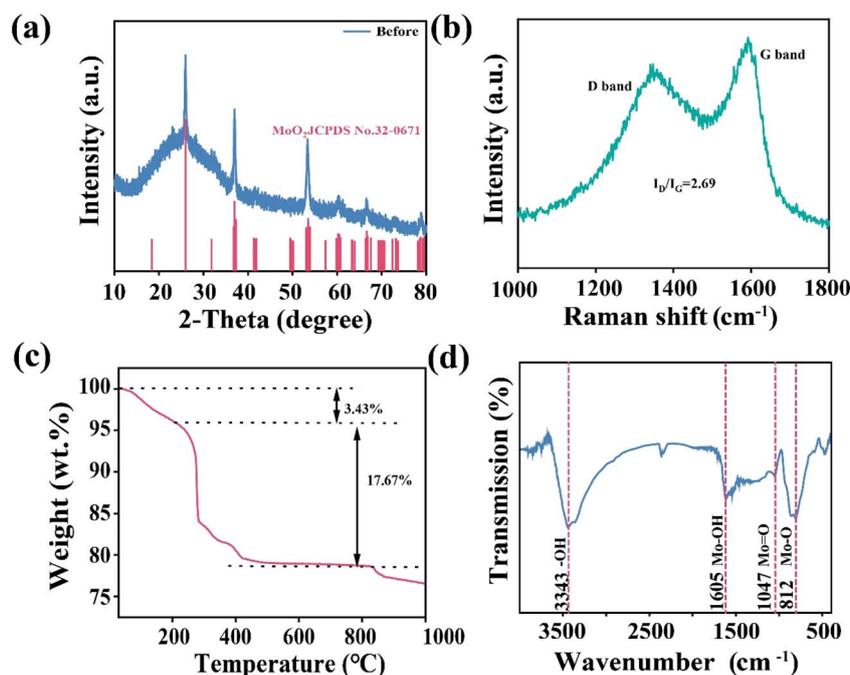

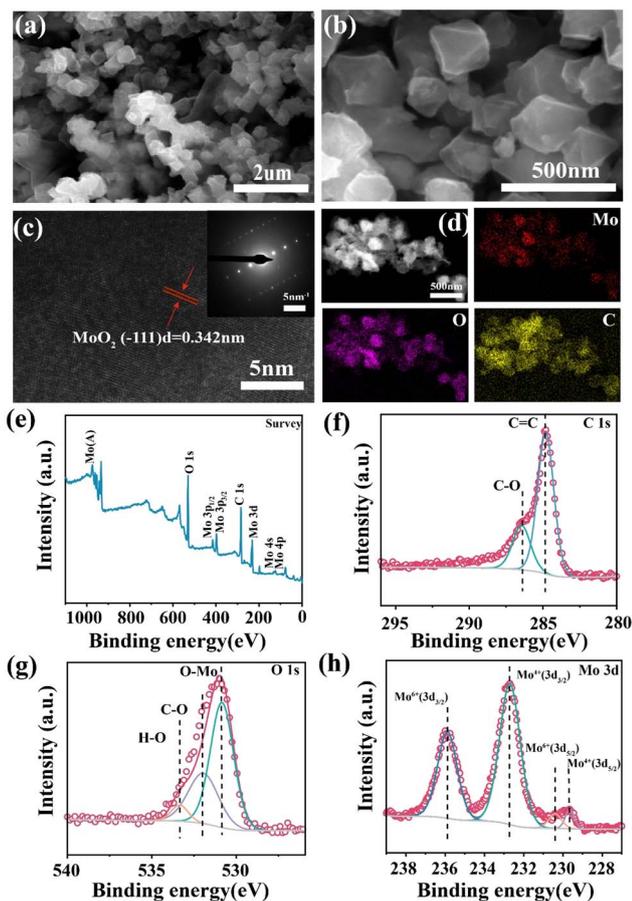Fig. 2 (a) XRD patterns, (b) Raman spectra, (c) TGA spectra, and (d) FTIR spectrum of MoO₂/C composite.
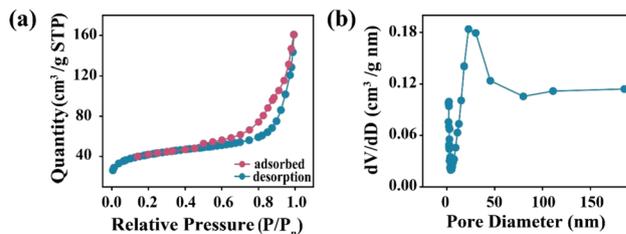
Fig. 4 (a) Nitrogen adsorption–desorption isotherms and (b) pore size distributions of MoO₂/C.

The specific BET surface area of the as-synthesized MoO_2/C was determined to be 137.2 m² g⁻¹ (Fig. 4). The nitrogen adsorption–desorption isotherm (Fig. 4a) can be classified as type IV, confirming the coexistence of mesopores and macropores in the material. Meanwhile, The BJH pore size distribution (Fig. 4b) reveals that MoO_2/C has a pore size range of 3–185 nm, with the majority centered between 14 and 45 nm, corresponding to the mesoporous range. According to previous studies, a high mesoporous ratio optimizes the porous structure by promoting U(VI) diffusion, significantly reducing diffusion resistance for uranyl ions, and minimizing pore blockage—thereby enhancing uranium(VI) adsorption.[38]

3.2. Uranium(VI) electroextraction measurement

An aqueous solution was employed to simulate nuclear waste-water, with uranyl ions as the primary salt constituent. The uranium removal performance of MoO_2/C electrodes was evaluated by batch CDI experiments using 60 mg L⁻¹ UO_2^{2+} aqueous solution. The CDI performance of MoO_2/C was investigated in a UO_2^{2+} aqueous solution (initial concentration: 60 mg L⁻¹) using batch-mode experiments. The electrosorption capacity
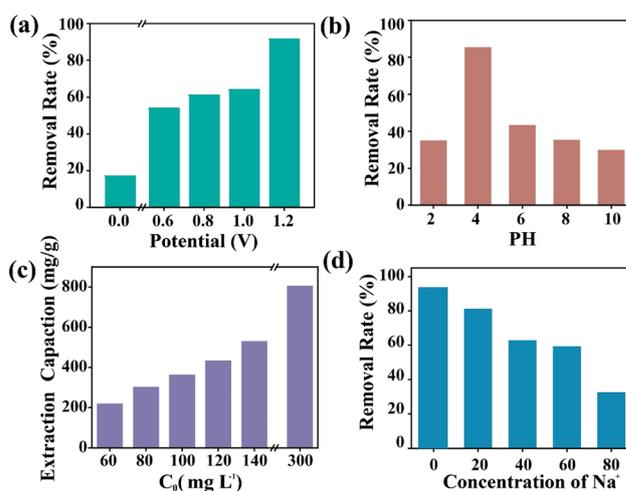

Fig. 5 Effect of (a) applied potential (pH = 4.0, T = 298 K, C_0 (U) = 60 mg L⁻¹, time = 5 h), (b) pH value (applied potential of 1.2 V, T = 298 K, C_0(U) = 60 mg L⁻¹, time = 5 h) on the electrosorption of U(VI) by MoO_2/C electrode. (c) The effect of initial U concentration, volume = 50 mL, time = 5 h. (d) Effect of concentration of Na⁺ on removal rate (C_0(U) = 60 mg L⁻¹, volume = 50 mL, time = 5 h).

Fig. 3 (a and b) SEM images of MoO₂/C composite with different magnification, (c) HRTEM image of MoO₂/C composite, (d) elemental mapping of Mo, O and C for MoO₂/C composite. (e) Overall XPS spectrum, (f) C 1s, (g) O 1s, and (h) Mo 3d spectra of MoO₂/C composite.

composite, which confirmed the homogeneous distribution of Mo, O, and C throughout the material.

XPS was conducted to analyze the surface chemical compositions and electronic properties of MoO_2/C. The XPS spectrumin Fig. 3e shows the existence of Mo, O and C elements. The strong C 1s spectrum could be fitted into two typical peaks (Fig. 3f) corresponding to C=C (284.8 eV) and C–O (286.4 eV), confirming the connection between MoO_2 and the carbon framework.[25,32,33] In the O 1s XPS spectrum (Fig. 3g), the peak observed at a binding energy of 530.8 eV is assigned to the Mo–O bond, while the two characteristic peaks appearing at 532.0 eV and 533.3 eV correspond to the C–O–C and C=O functional groups, respectively.[32,34] The peak of Mo 3d could be fitted into two doublets by applying the Gaussian fitting method (Fig. 3h). The peaks centered at 229.7 eV and 232.7 eV were attributed to the binding energies of Mo $3d_{5/2}$ and Mo $3d_{3/2}$ of Mo^{4+}, which were in agreement with previous reports.[35] The peaks centered at 230.3 and 235.8 eV corresponded to Mo $3d_{5/2}$ and $3d_{3/2}$ of Mo^{6+}, which probably resulted from the slight surface oxidation of MoO_2/C.[36,37]

The BET surface area and BJH pore size distribution were investigated using nitrogen adsorption–desorption isotherms.

(Q_e) and removal ratio of U(VI) in the CDI system were calculated using eqn (S1) and (S2).

A central question regarding the voltage-dependent U(VI) removal behavior of MoO_2/C (Fig. 5a) is whether the enhanced performance at higher applied voltages is primarily governed by faradaic reduction of U(VI) to U(IV) or by strengthened electrostatic adsorption of UO_2^{2+}. Although the removal efficiency increases markedly from 17% at 0 V to 91% at 1.2 V, ascribing this enhancement solely to either mechanism remains speculative. The 17% removal observed under open-circuit conditions points to a non-negligible contribution from surface functional groups. Considering that transition metal oxides readily develop hydroxyl-rich surfaces in aqueous solution, this adsorption behavior is reasonably attributed to inner-sphere coordination between Mo–OH groups on the MoO_2/C electrode and UO_2^{2+}, rather than to mere physical adsorption.[39,40] However, applying higher voltages will lead to water electrolysis (theoretical minimum: 1.23 V vs. SHE) and cause energy wastage.[41] Consequently, all further experiments were conducted at an applied voltage of 1.2 V.

As shown in the U(VI) speciation–pH diagram (Fig. S1), UO_2^{2+} predominates at pH 2.0. The pH-dependent U(VI) electrosorption by MoO_2/C was evaluated at 1.2 V (Fig. 5b). The removal ratio increased slightly from pH 2.0 to 4.0, then declined continuously from pH 4.0 to 10.0. This trend closely follows the speciation of U(VI). In the pH range of 2.0–4.0, the dominant UO_2^{2+} cations are effectively attracted to the negatively charged cathode via electrostatic interaction. At pH 6, the main species shift to UO_2OH^+ and $(UO_2)_3(OH)_5^+$; despite retaining positive charge, their larger molecular size and lower charge density likely impair electrosorption. At pH 8–10, anionic species including $(UO_2)_3(OH)_7^-$, $UO_2(OH)_3^-$, and $UO_2(OH)_2$ become prevalent, leading to electrostatic repulsion and a sharp drop in removal.[42,43] Thus, MoO_2/C achieves optimal performance under weakly acidic conditions (pH ≈ 4), where UO_2^{2+} dominates and electrostatic adsorption is most efficient. This renders the electrode suitable for uranium removal from acidic wastewater such as mine drainage.

The concentration of uranium in mining wastewater typically ranges from a few to over 100 mg L^{-1}, depending on the extraction process. To evaluate the adsorption performance under realistic conditions, we investigated the effect of initial U(VI) concentration. As shown in Fig. 5c, the uranium removal capacity increased with the initial concentration, reaching 219.4, 302.8, 363.2, 433.9, 530.9, and 807.8 mg g^{-1} at 60, 80, 100, 120, 140, and 300 mg L^{-1}, respectively. The exceptionally high adsorption capacity of MoO_2/C suggests its strong potential for practical uranium-containing wastewater treatment, leading to significantly reduced adsorbent dosage and enhanced process cost-effectiveness.[44]

As shown in Fig. 5d, increasing the Na^+ concentration from 0 to 80 mg L^{-1} sharply reduced U(VI) removal from 91.5% to 31.5%, indicating strong competitive inhibition between Na^+ and UO_2^{2+} for binding sites on MoO_2/C.[45] The pronounced sensitivity to Na^+ suggests that competition is not limited to a subset of sites, but broadly involves the same binding pools accessible to UO_2^{2+}. Given that Mo–OH groups have been

identified as the primary U(VI) adsorption sites under open-circuit conditions, it is plausible that Na^+ preferentially interacts with these hydroxyl moieties, directly impeding UO_2^{2+} coordination.[41,46–48] This interpretation is consistent with the established affinity of alkali metal ions for hydroxyl-functionalized surfaces in aqueous environments.

In addition to abundant Na^+ ions, other metal cations such as K^+, Mg^{2+}, and Ca^{2+} are also present. Further studies were conducted to investigate the effects of these common ions on the electroadsorption of uranium by MoO_2/C. As shown in Fig. 6a, the U(VI) removal rates reached 88.8%, 89.4%, 87.7%, and 83.3% in the presence of Na^+, K^+, Mg^{2+}, and Ca^{2+}, respectively.[19,49] Due to electrostatic interactions, these cations compete with uranium species for adsorption sites on the MoO_2/C surface, thereby reducing the overall uranium adsorption efficiency. Generally, cations with a higher charge and a smaller ionic radius exhibit stronger electrostatic interactions with MoO_2/C, leading to a more pronounced inhibitory effect on uranium adsorption. This trend follows the order of Ca^{2+} > Mg^{2+} > K^+ > Na^+, indicating that the MoO_2/C electrode possesses superior selectivity for UO_2^{2+} over the other coexisting cations.[50]

The temperature-dependent electrosorption of uranyl ions (298–318 K) exhibited a marked increase in removal rate with rising temperature (Fig. 6b), driven by synergistic thermal effects: elevated temperature enhances mass transfer by reducing diffusion resistance both to and within the electrode, while also promoting interfacial charge transfer.[49,51] These combined mechanisms lower the activation energy and improve both adsorption kinetics and capacity.

Isotherm modeling across temperatures (Table S2) indicates that uranium uptake by MoO_2/C is better described by the
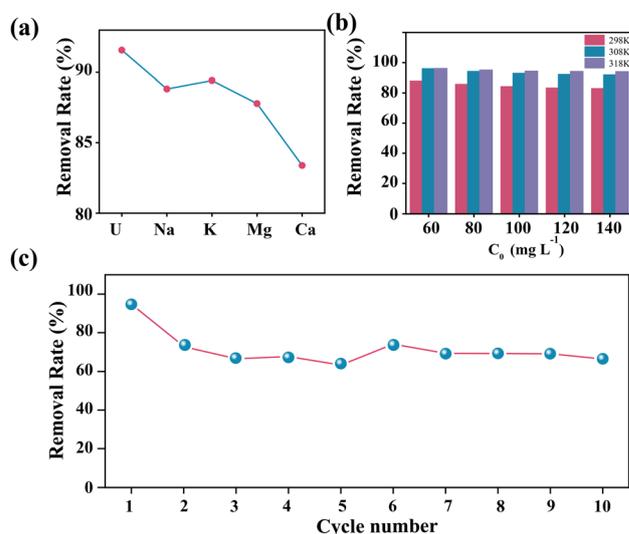

Fig. 6 (a) The removal performance of U(VI) by MoO_2/C in the presence of different cations (applied potential of 1.2 V, pH = 4.0, T = 298 K, C_0(U) = 60 mg L^{-1}, time = 5 h, coexisting ion concentration = 5 mmol L^{-1}) (b) effect of temperature on removal efficiency (298 K, 308K, 318 K) (c) reusability of MoO_2/C regarding electrosorption–desorption.

Freundlich model than by the Langmuir model, consistent with adsorption on a heterogeneous surface exhibiting multilayer characteristics. Despite this, the Langmuir model also provides a good fit and predicts a theoretical maximum adsorption capacity of 1018 mg g^{-1} under ambient conditions, further highlighting the material's promising potential for efficient uranium extraction.

Beyond removal efficiency, the electrochemical stability of the MoO$_2$/C electrode was evaluated through consecutive adsorption–desorption cycles using 0.1 mol L^{-1} Na$_2$CO$_3$ as the eluent (Fig. 6c). The electrode retained an average U(VI) removal rate above 65% over ten cycles, demonstrating good cycling stability.[52] Notably, the removal rate decreased from 91.5% in the first cycle to around 65% in the second cycle and remained stable thereafter. This plateau suggests the presence of two distinct types of binding sites on the MoO$_2$/C surface: reversible sites that allow efficient regeneration, and a fraction of irreversible or high-affinity sites that become permanently occupied after the initial cycle.[53] The stable 65% removal from cycle 2 onward likely reflects the sustained contribution of reversible sites, which are effectively regenerated by Na$_2$CO$_3$ elution.[54] This behavior is consistent with the partial site blockage observed in competitive adsorption studies and further supports the heterogeneous nature of the MoO$_2$/C surface.

Furthermore, low energy consumption was evaluated as a central advantage of the material, determining its practical potential. The energy-normalized removal of U(VI) (ENRU) and the energy consumption per unit mass (E) were determined from the monitored current during constant-voltage operation (1.2 V) using eqn (S3)–(S4) and (Fig. S2). After 5 hours at an initial UO$_2$$^{2+}$ concentration of 140 mg L^{-1}, the values were calculated to be 0.156 mg J^{-1} and 2.20 kWh kg^{-1}, respectively. The value is competitive with the most efficient electrosorption materials reported to date, such as electrochemical COF membranes (2.1 kWh kg^{-1})[55] and carbon-based electrodes (2.5–4.0 kWh kg^{-1}).[56,57] The excellent cycling stability and this remarkably low energy demand collectively position the material as a robust, economical, and viable candidate for practical uranium extraction from water.[41]

Electrosorption experiments were conducted to evaluate the uranium uptake performance at varying initial UO$_2$$^{2+}$ concentrations (Fig. 7a). The corresponding electrosorption isotherms were analyzed using both the Langmuir (eqn (S5)) and Freundlich (eqn (S6)) models. As summarized in Table S1, the Freundlich model provided a better fit to the experimental data than the Langmuir model, suggesting a multilayer adsorption mechanism. This behavior may be attributed to the presence of –OH functional groups on the MoO$_2$/C surface, which can interact weakly with uranyl ions, as well as the heterogeneous pore structure of the material. Nevertheless, the Langmuir model also exhibited a high correlation coefficient (R^2 = 0.9845), indicating that both physical and chemical adsorption mechanisms likely contribute to the electrosorption process. The actual maximum electrosorption capacity of MoO$_2$/C for U(VI) in a solution with an initial UO$_2$$^{2+}$ concentration of 300 mg L^{-1} was calculated to be 806.79 mg g^{-1}, substantially surpassing that of most reported adsorbents listed in Table S3.

To elucidate the electrosorption mechanism and identify the rate-controlling steps during the electrosorption process, the kinetic data (Fig. 7b–f) were fitted using three models: the
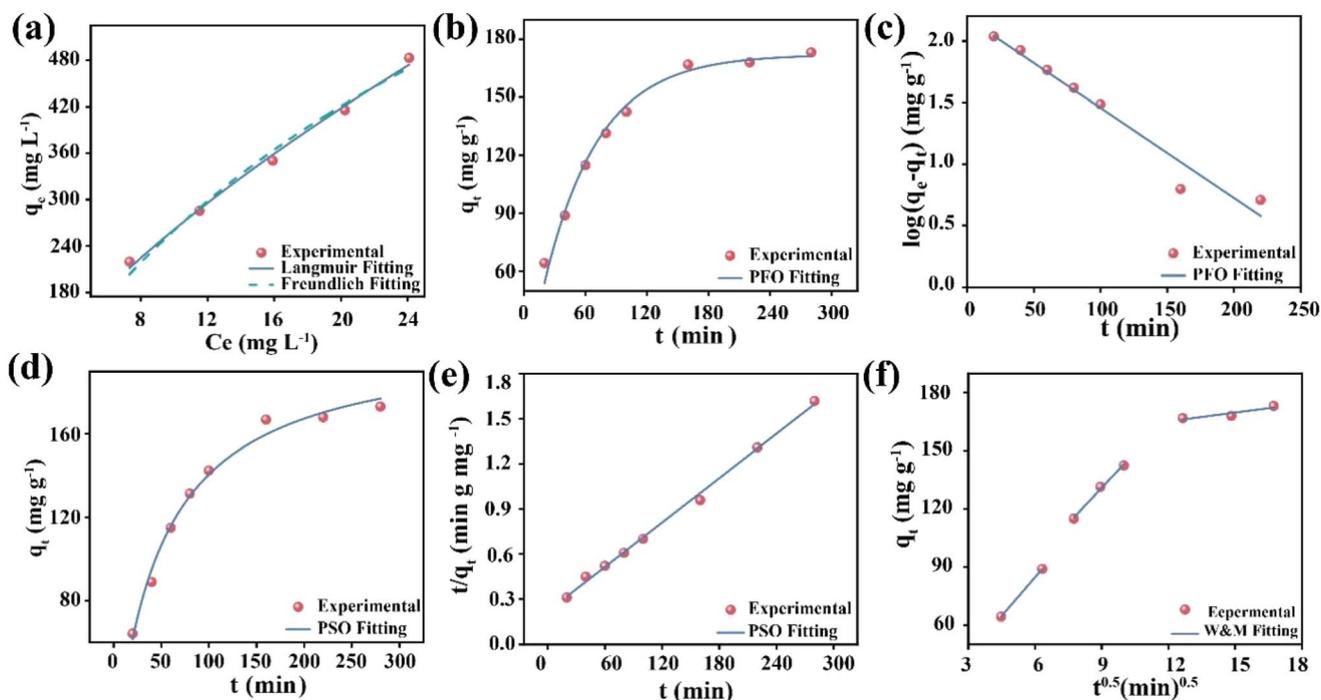

Fig. 7 (a) Adsorption isotherms of MoO$_2$/C electrode (applied potential:1.2 V, C_0(U) = 60, 80, 100, 120 and 140 mg L^{-1}, T = 298 K, 5 h running time); (b and c) the pseudo-first-order kinetic model (C_0(U) = 60 mg L^{-1}); (d and e) the pseudo-second-order kinetic model (C_0(U) = 60 mg L^{-1}), (f) Weber–Morris for electrosorption of U(VI) (C_0(U) = 60 mg L^{-1}).

pseudo-first-order kinetic model (PFO and eqn (S7)), the pseudo-second-order kinetic model (PSO and eqn (S8)), and the Weber–Morris intraparticle diffusion model (W&M and eqn (S9). The fitting results (listed in Table S4) suggest that the PSO model better describes the electrosorption kinetics of U(vi). Based on the fitting results, the electroadsorption rate of U(vi) is fully controlled by chemisorption, which involves electron sharing/transfer between the adsorbate and adsorbent, as well as chemical bonding of U(vi) to the active sites on the adsorbent surface. In addition, the Weber–Morris kinetic plots show that the electrosorption of UO_2^{2+} consists of three steps. Meanwhile, the calculated C values (intercept) were non-zero, indicating that the electrosorption may involve both physical and chemical adsorption processes.

3.3 Electrochemical characterization

The electrosorption capacity of CDI electrodes is governed by their electrochemical properties, such as conductivity and surface functional groups. Therefore, a systematic evaluation of the MoO₂/C composite's electrochemical properties was conducted in a conventional three-electrode cell. As shown in Fig. 8a, the CV curves recorded at scan rates from 5 to 80 mV s⁻¹ within a potential window of 0.1 to 0.56 V display a distinct rectangular shape. This shape is indicative of electric double layers (EDLs) that exhibit pseudocapacitive behavior.

Galvanostatic charge–discharge (GCD) measurements were conducted at various current densities (1, 2, and 5 A g⁻¹) to investigate the role of pseudocapacitance in the capacitive deionization (CDI) process (Fig. 8b). At a scan rate of 5 mV s⁻¹, the MoO₂/C hybrid demonstrates a specific capacitance of 10.3 F g⁻¹ (eqn (S10) and Fig. 8c), reflecting limited charge storage performance under quasi-static electrochemical conditions. Given this comparatively low capacitance relative to other electrode materials, the remarkable electrosorption performance of MoO₂/C suggests contributions beyond the conventional electric double-layer (EDL) mechanism, highlighting the significant involvement of pseudocapacitive processes.[58]
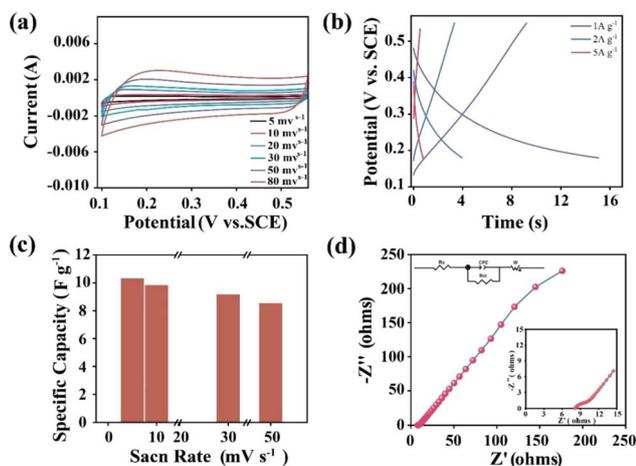
Nyquist plots with equivalent circuit fitting for the MoO₂/C composite (Fig. 8d) reveal its distinctive impedance characteristics. The absence of discernible semicircles in the medium–high frequency region implies negligible charge transfer resistance (R_{ct}), while the nearly vertical low-frequency trend with minimal deviation from the imaginary axis ($-Z''$) reflects ideal capacitive behavior akin to high-performance supercapacitors. Circuit fitting confirms low resistance values ($R_s = 8.12\ \Omega$, $R_{ct} = 1.71\ \Omega$), consistent with excellent conductivity and efficient charge transfer.[19,51] This enhanced electrical performance is attributed to the percolating network of sp²-hybridized carbon within the conductive matrix, which facilitates continuous electron transport pathways across the composite.[59]

3.4. Uranium(vi) removal mechanism

The electrosorption of U(vi) from aqueous solutions typically proceeds through five dominant mechanisms: (i) electrical double-layer (EDL) formation, (ii) pseudocapacitive interactions, (iii) surface complexation, (iv) electroreduction, and (v) electrolytic deposition. To elucidate the adsorption pathways in the as-synthesized MoO₂/C nanocomposite, we performed multi-technique post-analysis of the electrode after capacitive deionization (CDI) operation, combining advanced characterization methods to establish structure–property relationships.

The as-synthesized MoO₂/C demonstrates remarkable structural stability throughout the CDI process. Post-adsorption characterization confirms the preservation of the octahedral architecture, with SEM images (Fig. 9a and b) showing maintained morphological integrity. XRD analysis of the spent adsorbent (Fig. S3) reveals characteristic uranium signatures, suggesting partial reduction of U(vi) species. Phase identification unambiguously establishes the formation of non-stoichiometric uranium dioxide (UO₂.₉, JCPDS no. 49-1389), providing direct evidence for the partial electrochemical reduction of UO_2^{2+} to UO₂.₉ during the electrosorption process. Elemental mapping (Fig. 9c) further verifies homogeneous distribution of uranium across the composite surface, collectively demonstrating successful uranyl ion immobilization on the MoO₂/C substrate.

To unravel the removal mechanism of UO_2^{2+} by MoO₂/C, we systematically investigated the material's structural and chemical evolution using integrated characterization techniques (XRD, FTIR, XPS) following electroadsorption. The surface chemical evolution of MoO₂/C before and after electroadsorption was investigated by FTIR spectroscopy (Fig. 9d). The spectrum exhibits characteristic bands at 1605 cm⁻¹ (orange dashed line) and 3343 cm⁻¹ (black dashed line), corresponding to Mo–OH bending vibrations and O–H stretching of adsorbed water molecules, respectively.[37,44] These features confirm the presence of abundant surface hydroxyl groups that facilitate uranyl (UO_2^{2+}) adsorption through complexation.

Following electroadsorption, the emergence of a new peak at 868 cm⁻¹ is assigned to the asymmetric stretching vibration of O=U=O, confirming successful UO_2^{2+} immobilization. Notably, the newly observed absorptions at 1125.6 cm⁻¹ and 1033 cm⁻¹ are characteristic of Mo–O–U bridging vibrations,
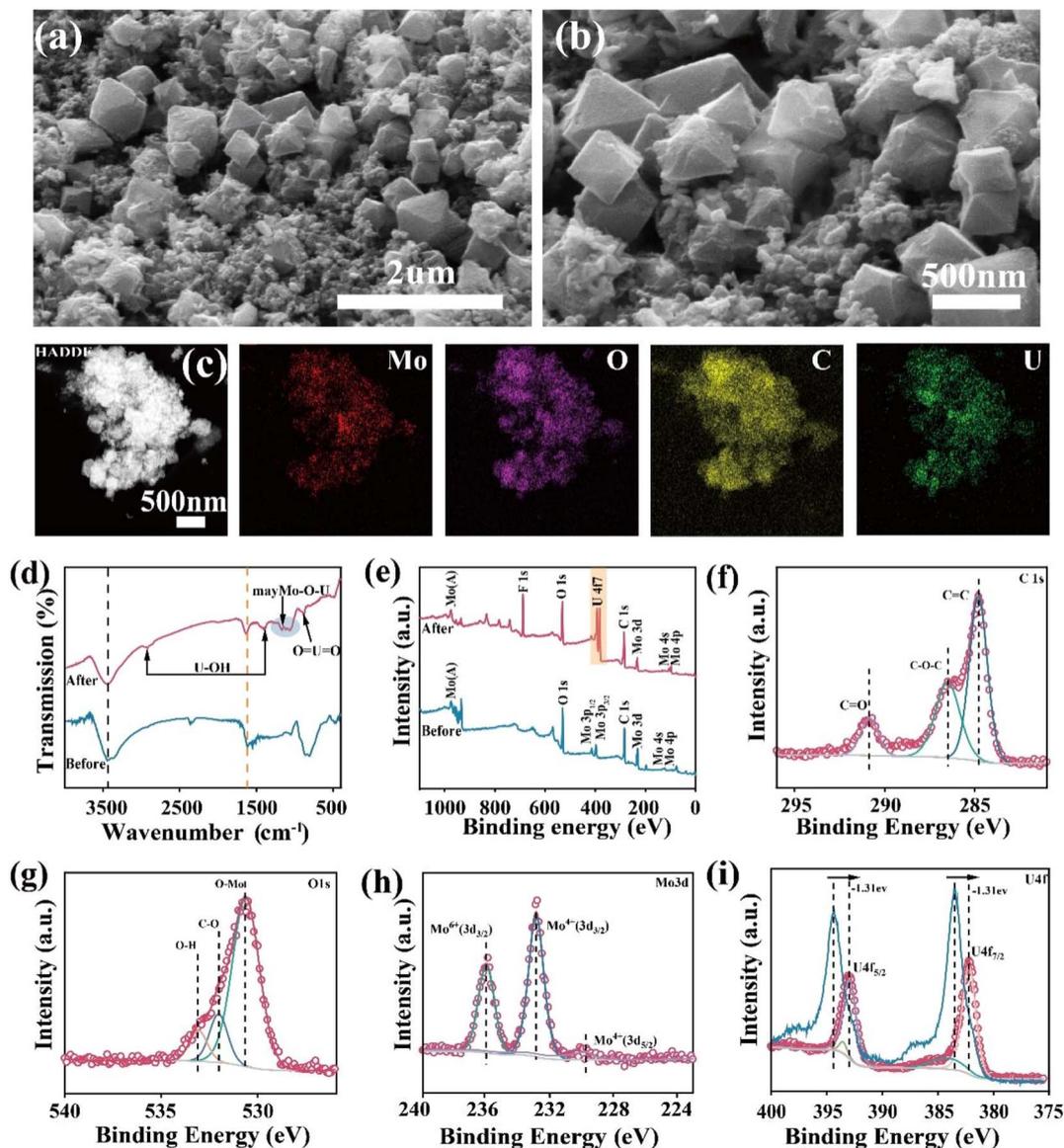

Fig. 8 (a) CV, (b) GCD, (c) specific capacity, and (d) Nyquist curves and fitting circuit of the MoO₂/C.

Fig. 9 (a and b) SEM and (c) HADDF and EDS mappings of MoO_2/C (d) FTIR spectra comparation of MoO_2/C before after electrosorption (e) survey XPS spectrum of MoO_2/C before after electrosorption (f) C 1_s (g) O 1s (h) Mo 3d and (i) U 4f spectral comparison of MoO_2/C after electroadsorption *versus* uranyl nitrate.

demonstrating chemical bonding between uranium and the molybdenum oxide framework rather than mere physical adsorption.[60,61]

The U(VI) electroadsorption mechanism on MoO_2/C electrodes was elucidated through comparative XPS analysis. The survey spectrum (Fig. 9e) confirms the pristine electrode contains only Mo, O, and C elements, while the emergence of U 4f doublet in post-adsorption samples unequivocally demonstrates uranium immobilization. The detected F1s signal is ascribed to the PVDF binder employed in electrode preparation.[41]

High-resolution spectra (Fig. 9f) provide further insight into chemical states: The C1s spectrum deconvolutes into characteristic C=C (284.8 eV) and C–O–C (286.4 eV) components maintaining stable positions after electroadsorption.[44] Notably, the appearance of a new C1s peak at 290.88 eV suggests possible

PVDF decomposition forming CF_3COOH species.[62] However, the cycling stability data demonstrate that this binder decomposition does not significantly compromise electrode performance over 10 cycles, with the uranium removal efficiency stabilizing at approximately 65% following initial activation. This indicates that the extent of PVDF degradation is limited and does not substantially affect the structural integrity or electrochemical activity of the MoO_2/C composite under the tested conditions.[63] For longer-term operation, alternative binders such as carboxymethyl cellulose (CMC) or Nafion could be considered to enhance chemical stability.[64,65] Additionally, optimizing the binder content or introducing cross-linking agents may mitigate decomposition while maintaining electrode mechanical integrity. Additional high-resolution analysis of O1s, Mo3d and U4f core levels reveals binding energy shifts
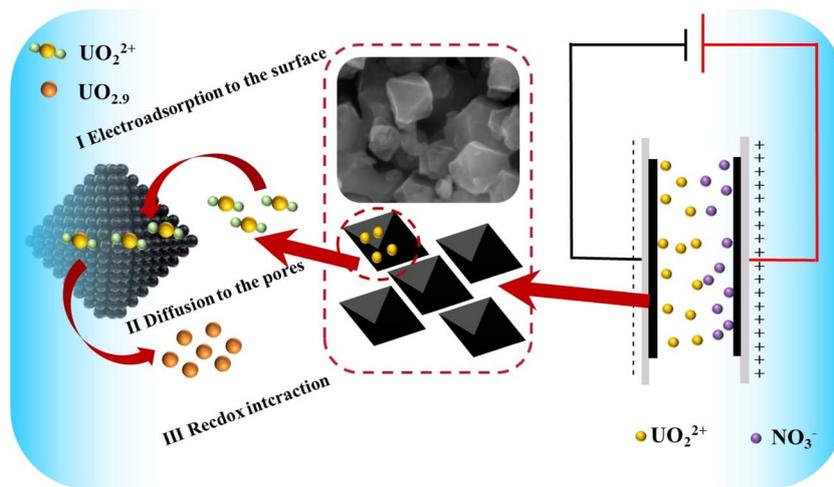
Fig. 10 The mechanism of MoO_2/C in removing uranyl.

indicating chemical interactions between uranium species and the MoO_2/C substrate.

After uranium electroadsorption, the O 1s XPS spectrum reveals a prominent peak at 530.6 eV, attributed to the Mo–O bond (Fig. 9g).[25,35] Two additional peaks at 532.0 eV and 533.1 eV correspond to C–O–C and C=O functionalities, respectively.[66,67] Notably, the Mo–O binding energy shifts downward by 0.2 eV, suggesting a chemical interaction between UO_2^{2+} (U^{6+}) and the MoO_2/C surface, likely involving electron donation from the MoO_2/C matrix to the uranyl species. In the Mo 3d region, characteristic doublets at 229.7 eV ($3d_{5/2}$) and 232.8 eV ($3d_{3/2}$) are observed, consistent with Mo^{4+} oxidation state (Fig. 9h).[68]

The adsorption of uranyl ions (UO_2^{2+}), acting as strong electron-deficient Lewis acids, onto the MoO_2/C surface involves electron transfer from Mo^{4+} species. This donation reduces the electron density in Mo 3d orbitals and increases the effective nuclear charge, selectively shifting the Mo^{4+} $3d_{3/2}$ binding energy by +0.14 eV while the Mo^{4+} $3d_{5/2}$ peak remains unchanged at 229.7 eV. During the partial reduction of uranyl species ($UO_2^{2+} \rightarrow UO_{2.9}$), Mo^{4+} serves as an electron donor, with its continued binding energy increase providing direct evidence for this charge transfer mechanism. Concurrently, the Mo^{6+} $3d_{3/2}$ main peak exhibits a +0.15 eV shift accompanied by the disappearance of its satellite peak at 230.3 eV. These spectral modifications confirm the formation of Mo–O–U bridging bonds or direct Mo–U interactions, where the resultant chemical bonding significantly modulates the local electronic environment of Mo sites, collectively explaining the observed binding energy shifts and satellite peak disappearance.[69,70]

XPS analysis of MoO_2/C after electroadsorption reveals well-defined U 4f doublet peaks (Fig. 9i), confirming successful U(VI) immobilization. The emergence of $UO_{2.9}$ peaks in the XRD pattern of MoO_2/C (Fig. S3) provides direct evidence for the partial reduction of uranyl species during electrosorption. $UO_{2.9}$, as a non-stoichiometric oxide, indicates that a fraction of U(VI) has been reduced to lower valence states, likely U(IV), while the bulk phase retains an overall oxidized lattice. High-

resolution U4f XPS spectra display characteristic U^{6+} signatures, with primary peaks at 382.2 eV ($4f_{7/2}$) and 393.0 eV ($4f_{5/2}$), accompanied by satellite features at 384.7 eV and 393.5 eV.[1,38,71] The satellite peaks from charge transfer within uranyl species confirm that U(VI) predominates at the electrode surface. Combined XRD and XPS analyses indicate partial reduction in the near-surface region, while the outermost layer remains U(VI).[72] This aligns with an electrosorption mechanism involving both electrostatic accumulation and concomitant mild reduction. Additionally, the coordination complexation between uranium species and surface hydroxyl groups drives electron transfer during electrosorption, reducing the binding energy of uranium by 1.31 eV and consequently leading to the reduction of uranyl to uranium oxides—a mechanism confirmed by this significant energy shift.[73]

Based on the above analysis, the electrosorption mechanism of UO_2^{2+} on MoO_2/C is illustrated in Fig. 10. Electrochemical reduction promotes the adsorption of uranyl ions and offers a new approach for uranium enrichment. Initially, electrostatic attraction between the MoO_2/C surface and UO_2^{2+} ions facilitates their rapid transfer to the material surface. Secondly, the porous structure of MoO_2/C provides abundant adsorption sites for UO_2^{2+} ions, enhancing their diffusion and retention within the material. Furthermore, during the electrodeposition process under an applied electric field, UO_2^{2+} ions exhibit a strong reduction potential and a tendency to adhere to the electrode surface. The application of a 1.2 V voltage enables the partial reduction of UO_2^{2+} to $UO_{2.9}$ on the MoO_2/C cathode, followed by its deposition, thereby achieving a high electrosorption removal rate.

4 Conclusion

This study presents a MOF-assisted synthesis strategy for fabricating porous MoO_2/C nano-octahedra composed of ultrafine nanocrystals, with systematic evaluation of their U(VI) adsorption performance. The material demonstrates exceptional uranium adsorption capacity (806.79 mg g^{-1}),

remarkable selectivity, and excellent cycling stability in aqueous solutions. The adsorption process follows pseudo-second-order kinetics and the Freundlich isotherm model, indicating multilayer chemisorption characteristics. Mechanistic studies reveal that uranium uptake proceeds through three primary pathways: electrostatic interactions, surface complexation, and redox transformation between U(VI) and Mo(VI). This work establishes a novel synthetic paradigm and provides theoretical foundations for developing high-performance uranium extraction materials.

Author contributions

Hongyan Zhou: writing – original draft, investigation. Suyuan Zhen: supervision, writing – review & editing. Ranran Jiao, Xiaotong Ma,Yuwei Mi: discussion.

Conflicts of interest

There are no conflicts to declare.

Data availability

The authors confirm that the data supporting the findings of this study are available within the article.

Supplementary (SI) information is available. See DOI: https://doi.org/10.1039/d6ra00643d.

Acknowledgements

References

1 M. Cao, L. Chen, W. Xu, J. Gao, Y. Gui, F. Ma, P. Liu, Y. Xue and Y. Yan, *J. Water Process Eng.*, 2022, **48**, 102930.

2 C. Liu, K. Xuan, Y. Guo, H. Jiang, W. Ma, X. Wang, Z. Zhou, J. Li and Y. Guo, *J. Hazard. Mater.*, 2025, **491**, 137878.

3 A. C. M. Lamb, F. Grieser and T. W. Healy, *Colloids Surf., A*, 2016, **499**, 156–162.

4 H. Guo, E. Hu, Y. Wang, Z. Ou, B. Huang, J. Lei, H. Liu, R. He and W. Zhu, *Nat. Commun.*, 2025, **16**, 2012.

5 Y. Yuan, Q. Yu, M. Cao, L. Feng, S. Feng, T. Liu, T. Feng, B. Yan, Z. Guo and N. Wang, *Nat Sustainability*, 2021, **4**, 708–714.

6 D. Mei, L. Liu and B. Yan, *Coord. Chem. Rev.*, 2023, **475**, 214917.

7 E. Calì, J. Qi, O. Preedy, S. Chen, D. Boldrin, W. R. Branford, L. Vandeperre and M. P. Ryan, *J. Mater. Chem. A*, 2018, **6**, 3063–3073.

8 Z. Gao, S. Chen, H. Ding, Y. Song, Z. Li, H. Wang, H. Wu, H. Li and Y. Su, *Inorg. Chem. Commun.*, 2022, **146**, 110134.

9 Y. Zhang, S. Huang, B. Mei, L. Jia, J. Liao and W. Zhu, *Sci. Total Environ.*, 2023, **881**, 163525.

10 L. Zhang, Y.-T. Luo, S.-J. Xiao, J.-Q. Fan, Q.-G. Tan, C. Sun, A.-M. Song, R.-P. Liang and J.-D. Qiu, *Chem. Commun.*, 2024, **60**, 3583–3586.

11 Y. Ye, B. Fan, Z. Qin, X. Tang, Y. Feng, M. Lv, S. Miao, H. Li, Y. Chen, F. Chen and Y. Wang, *J. Hazard. Mater.*, 2022, **432**, 128723.

12 Q. Hu, D. Wang, J. Liang, Z. Liu and J. Li, *Sep. Purif. Technol.*, 2024, **330**, 125494.

13 S. Yang, Z. Ye, X. Cheng, Y. Wang, Z. Luan, W. Li and B. Hu, *Chem. Eng. J.*, 2023, **474**, 145598.

14 J. Zhang, D. Liu, X. Wang, Z. Zheng, J. Hu and Z. Chen, *J. Mol. Liq.*, 2025, 419.

15 A. Tyagi, H. Sharma, A. K. Yadav, P. Singhal, G. Karmakar, D. Bhattacharyya and S. K. Jha, *Ind. Eng. Chem. Res.*, 2024, **63**, 10892–10902.

16 S. Sun, D. Xiong, Y. Zhuang, G. Cheng, L. Shi and Y. Zhang, *Environ. Technol. Innovat.*, 2022, **28**, 102779.

17 Y. Xue, M. Cao, J. Gao, Y. Gui, J. Chen, P. Liu, F. Ma, Y. Yan and M. Qiu, *Sep. Purif. Technol.*, 2021, **255**, 117753.

18 H. Jin, Y. Hu, Z. Shen, H. Pan, H. Bao, L. Yin, G. Zhao, Z. Ji, X. Wang and X. Huang, *Nat. Commun.*, 2025, **16**, 3574.

19 Y. Zhang, J. Zhou, D. Wang, R. Cao and J. Li, *Chem. Eng. J.*, 2022, **430**, 132702.

20 I. Raza, M. Hussain, A. N. Khan, T. Katzwinkel and J. Feldhusen, *Int. J. Lightweight Mater. Manuf.*, 2021, **4**, 195–202.

21 S. Gupta, *Discov. Mater.*, 2025, **5**, 262.

22 M. Sharma, P. Dhiware, H. Laddha, V. C. Janu and R. Gupta, *Coord. Chem. Rev.*, 2024, **508**, 215766.

23 S. R. Panda, S. Upadhyay, R. Priya, A. Chandel and O. P. Pandey, *Chem. Phys.*, 2026, **603**, 113071.

24 J. Zhu, X. Zuo, X. Chen and Y. Ding, *Synth. Met.*, 2021, **280**, 116872.

25 J. Chen, X. L. Chen, R. Lu, Y. Li and A. Q. Pan, *Rare Met.*, 2023, **42**, 2592–2600.

26 Z. Amiri, H. Banna Motejadded Emrooz and M. Safarzadeh Khosrowshahi, *Sci. Rep.*, 2025, **15**, 22086.

27 H. Hu, J. Xu, C. Deng and X. Ge, *Mater. Res. Bull.*, 2014, **51**, 402–410.

28 C. Q. Sun, *Prog. Mater. Sci.*, 2009, **54**, 179–307.

29 N. R. Reddy, P. M. Reddy, T. K. Mandal, K. R. Reddy, N. P. Shetti, T. A. Saleh, S. W. Joo and T. M. Aminabhavi, *J. Environ. Manage.*, 2021, 298.

30 Y. Wang and X. Meng, *ACS Sustain. Chem. Eng.*, 2024, **12**, 12997–13006.

31 X. H. Yongming Sun, W. Luo and Y. Huang, *ACS Nano*, 2011, **5**, 7100–7107.

32 B. Huang, S. Liu, X. Zhao, Y. Li, J. Yang, Q. Chen, S. Xiao, W. Zhang, H.-E. Wang and G. Cao, *Sci. China Mater.*, 2020, **64**, 85–95.

33 Z. Kou, T. Wang, Q. Gu, M. Xiong, L. Zheng, X. Li, Z. Pan, H. Chen, F. Verpoort, A. K. Cheetham, S. Mu and J. Wang, *Adv. Energy Mater.*, 2019, **9**, 1803768.

34 D. Zhao, J. Qin, L. Zheng and M. Cao, *Chem. Mater.*, 2016, **28**, 4180–4190.

35 H. Si, L. Sun, Y. Zhang, L. Wu, Y. Zhang and Y. Zhang, *Dalton Trans.*, 2020, **49**, 1637–1645.

36 C. Zhang, L. Wang, Z. Cao, R. Li and S. Ye, *Chem. Commun.*, 2024, **60**, 2744–2747.

37 S. Jing, X. Xiao, Z. Liu, M. Ma and Q. Li, *J. Taiwan Inst. Chem. Eng.*, 2024, **157**, 105444.

38 Y. Yu, J. Liu, Q. Liu, Y. Xue, R. Chen, J. Yu, J. Zhu and J. Wang, *ACS Appl. Mater. Interfaces*, 2024, **16**, 49778–49789.

39 D. Liu, Y. Wang, L. Zuo, M. Guo and S. Liu, *Front. Mater.*, 2025, **12**, 1541204.

40 C. Meng, W. Shu, K. Zhao, C. Yan, Z. Li, Q. Wei, M. Wang, Y. Liu and Z. Zhang, *Inorg. Chem.*, 2023, **62**, 8969–8979.

41 R. Jiao, Z. Chen, S. Zeng, D. Wang and J. Li, *J. Environ. Chem. Eng.*, 2023, **11**, 111275.

42 X. Li, J. Huang, Z. Shi, Y. Xie, Z. Xu, J. Long, G. Song, Y. Wang, G. Zhang, X. Luo, P. Zhang, S. Zha and H. Li, *J. Environ. Manage.*, 2023, **342**, 118088.

43 D. Wang, Y. Xu, D. Xiao, Q. Qiao, P. Yin, Z. Yang, J. Li, W. Winchester, Z. Wang and T. Hayat, *J. Hazard. Mater.*, 2019, **371**, 83–93.

44 Y. T. Baheri, M. A. Hedayati, M. Maleki, H. Karimian, A. Shokrieh, M. M. Shokrieh, A. Imani and Y. Tong, *J. Power Sources*, 2025, **645**, 237099.

45 S. Goldberg, *Soil Sci.*, 2010, **175**, 105–110.

46 R. Jiao, S. Zeng and J. Li, *Sep. Purif. Technol.*, 2025, **359**, 130436.

47 D.-B. Ji, S.-X. Hao, X.-Q. Fan, R.-L. Liang, Z.-Q. Qiao, Z.-H. Bai, D.-Q. Ji, Q.-H. Gao and H.-J. Wu, *Dalton Trans.*, 2024, **53**, 5020–5033.

48 M. Hao, Y. Xie, X. Liu, Z. Chen, H. Yang, G. I. N. Waterhouse, S. Ma and X. Wang, *JACS Au*, 2023, **3**, 239–251.

49 R. Cao, J. Zhang, D. Wang, F. Sun, N. Li and J. Li, *Chem. Eng. J.*, 2023, **461**, 142080.

50 M. Su, T. Ou, J. Li, L. Tong, W. Han, Y. Wu and D. Chen, *J. Environ. Chem. Eng.*, 2023, **11**, 109471.

51 Q. Liu, N. Wang, B. Xie and D. Xiao, *Sep. Purif. Technol.*, 2023, **308**, 122866.

52 H. Wang, C. Cao, J. Chen, G. Zhou, T. Liu, Y. Yuan and N. Wang, *Nat. Commun.*, 2025, **16**, 10799.

53 J. Shang, C. Liu, Z. Wang and J. Zachara, *Water Resour. Res.*, 2014, **50**, 855–870.

54 E. A. Santos and A. C. Q. Ladeira, *Environ. Sci. Technol.*, 2011, **45**, 3591–3597.

55 C.-R. Zhang, J.-X. Qi, W.-R. Cui, X.-J. Chen, X. Liu, S.-M. Yi, C.-P. Niu, R.-P. Liang and J.-D. Qiu, *Chem*, 2022, **66**, 562–569.

56 S. K. Raj, A. J. Carrier, B. C. Youden, M. R. Servos, K. D. Oakes and X. Zhang, *Chem. Eng. J.*, 2024, **492**, 152341.

57 B. Xue, Y. Ji, H. Yi, Y. Liu, X. Huang, C. Liu, J. Li, R. Xiao and X. Tian, *Adv Funct*, *Mater*, 2026, DOI: 10.1002/adfm.202529094.

58 Y. Liu, X. Tang, L. Zhou, Z. Liu, J. Ouyang, Y. Dai, Z. Le and A. A. Adesina, *Sep. Purif. Technol.*, 2022, **290**, 120827.

59 H. B. Wu, B. Y. Xia, L. Yu, X.-Y. Yu and X. W. Lou, *Nat. Commun.*, 2015, **6**, 6512.

60 E. Grabias and M. Majdan, *J. Radioanal. Nucl. Chem.*, 2017, **313**, 455–465.

61 Q. Xin, H. Wang, E. Hu, K. Luo, Z. Lei, F. Hu, X. Liu, J. Hu and Q. Wang, *Desalination*, 2025, **606**, 118768.

62 L. Zhang, H. Gao, Y. Zhu, I. Tran, W. Tang, J. Lin, A. U. Mu, J. Wu, W. Li, D. Nordlund, L. Mu and Z. Chen, *Adv. Energy Mater.*, 2025, **15**, 2406084.

63 X. Zhao, S. Niketic, C.-H. Yim, J. Zhou, J. Wang and Y. Abu-Lebdeh, *ACS Omega*, 2018, **3**, 11684–11690.

64 J. Li, Q. Chen, B. Pang, X. Tan, M. Fang and B. Ma, *Sustain. Carbon Mater.*, 2026, **2**, e001.

65 D. Alvira, D. Antorán and J. J. Manyà, *J. Energy Chem.*, 2022, **75**, 457–477.

66 Y. Zhang and Y. He, *Water*, 2025, **17**, 2814.

67 A. Thinthasit, P. Kantang, I. M. Khoris, D. Nugroho, J. Lee, R. Benchawattananon and C. Poonsawat, *Sci. Rep.*, 2025, **15**, 20722.

68 G. Greczynski and L. Hultman, *Prog. Mater. Sci.*, 2020, **107**, 100591.

69 T. C. Taucher, I. Hehn, O. T. Hofmann, M. Zharnikov and E. Zojer, *J. Phys. Chem. C*, 2016, **120**, 3428–3437.

70 Y. Zhang, J. Xu, S. Lu, H. Li, T. Yonar, Q. Hua, T. Liu and Y. Zhang, *Adv. Compos. Hybrid Mater.*, 2025, **8**, 108.

71 X. Yuan, C. Yin, Y. Zhang, Z. Chen, Y. Xu and J. Wang, *Sci. Rep.*, 2019, **9**, 5807.

72 S. Li, L. Zhao, S. Wang, C. Li, L. Cai, S. Lv and G. Wang, *Chem. Eng. J.*, 2024, 499.

73 C. Yan, Y. Liao, C. Shen, X. Weng, R. Lei, C. Liao, Y. Zhou and M. Wang, *Chem. Eng. J.*, 2023, **461**, 142012.